



Soft Matter

**Quantification of Functional Crosslinker Reaction Kinetics
via Super-resolution Microscopy of Swollen Microgels**

Journal:	<i>Soft Matter</i>
Manuscript ID	SM-ART-08-2019-001618.R1
Article Type:	Paper
Date Submitted by the Author:	23-Oct-2019
Complete List of Authors:	Karanastasis, Apostolos; Rensselaer Polytechnic Institute, Materials Science and Engineering Kenath, Gopal; Rensselaer Polytechnic Institute, Materials Science and Engineering Sundararaman, Ravishankar; Rensselaer Polytechnic Institute, Materials Science and Engineering Ullal, Chaitanya; Rensselaer Polytechnic Institute, Materials Science and Engineering

SCHOLARONE™
Manuscripts

Cite this: DOI: 00.0000/xxxxxxxxxx

Quantification of Functional Crosslinker Reaction Kinetics via Super-resolution Microscopy of Swollen Microgels[†]

Apostolos A. Karanastasis,^{a‡} Gopal S. Kenath,^{a‡} Ravishankar Sundararaman^a and Chaitanya K. Ullal^{*a}

Received Date

Accepted Date

DOI: 00.0000/xxxxxxxxxx

Super resolution microscopy (SRM) brings the advantages of optical microscopy to the imaging of nanostructured soft matter, and in colloidal microgels, promises to quantify variations of crosslink densities at unprecedented length scales. However, the distribution of all crosslinks does not coincide with that of dye-tagged crosslinks, and density quantification in SRM is not guaranteed due to over/under-counting dye molecules. Here we demonstrate that SRM images of microgels encode reaction rate constants of functional cross linkers, which hold the key to correlating these distributions. Combined with evolution of microgel particle radii, the functional cross linker distributions predict consumption versus time with high fidelity. Using a Bayesian regression approach, we extract reaction rate constants for homo and cross propagation of the functional crosslinker, which should be widely useful for predicting spatial variations in crosslink density of gels.

1 Introduction

Super-resolution microscopy (SRM),^{1,2} which refers to the ability of far-field fluorescence microscopy to resolve objects with separations smaller than the diffraction limit by separating their detection in time, is increasingly being applied to areas of soft matter beyond that of the biological sciences.³ Early demonstrations of the benefits of moving optical microscopy to the relevant nanometer length scales for polymers and colloids included the ability to provide 3D structural information,⁴ particularly in solvent swollen environments that are otherwise challenging to image in;⁵ reveal microstructure of multiple phases through multi-color imaging;⁶ capture dynamic processes;^{7–9} and yield environmental information such as pH¹⁰ and orientation and alignment of chains¹¹. Recently, there has been particular interest in the application of SRM to thermoresponsive colloidal polymer gels, or microgels, since imaging this material system leverages all of the aforementioned advantages.^{12–15}

More challenging to adopt has been the extraction of information based on the quantification of molecular distributions, one of the main goals of molecular analysis with SRM and an active

area of research¹⁶. Errors in quantification arise primarily due to variations in labeling efficiency, and under or over counting due to variations in the photo-physical behavior of fluorophores.

Quantification of molecular distributions on the nano and micro scales is of fundamental scientific importance to gels, especially those synthesized by free radical polymerization, due to the presence of spatial variations in crosslink density on these length-scales. These heterogeneities are often markedly pronounced in poly(*n*-isopropylacrylamide), or PNiPAM, gels and microgels copolymerized with *N,N'*-methylenebisacrylamide (BIS) as the crosslinker. A notable advance has been the invention of dye tagged crosslinkers and the super-resolution imaging of gels and microgels containing trace quantities of these functional crosslinkers.^{17,18} The utility of these molecules is exemplified by the finding¹⁷ that the core regions of individual microgels need not be spherically symmetric as they are known to be at the ensemble level from scattering studies¹⁹. Instead, they can contain within their already dense microgel cores, deca-nanosized regions of higher crosslink density¹⁷ that are non-thermoresponsive^{20,21}.

The continued promise of these new crosslinkers includes revealing how crosslink distributions in the swollen state correlate with properties - mechanical, transport and optical - under both static and dynamic conditions. This potential will be maximized if the spatial distributions of the functional crosslinkers can be correlated with those of the monomers that are not imaged by SRM, which in turn requires the establishment of reaction rate constants of the new molecules, as described below.

For NiPAM microgels, which are the focus of this paper, it is

^a Department of Materials Science and Engineering, Rensselaer Polytechnic Institute, 110 8th Street, Troy, New York 12180, USA; E-mail: ullal@rpi.edu

[†] Electronic Supplementary Information (ESI) available: [Detailed list of materials and reagents; molecular synthesis and characterization details; additional DLS results; additional info and graphs on rate constant determination]. See DOI: 10.1039/cXsm00000x/

[‡] These authors contributed equally to this work

known that the spatial distribution of any given monomer residue of microgels in their collapsed form is a direct function of the consumption of the respective monomer during synthesis^{22–24}. These spatial distributions can be semi-quantitatively predicted by a terminal copolymerization model that uses as input the absolute kinetic reaction rate constants for homopropagation and crosspropagation for each pair of monomers involved in the polymerization reaction.²³ This model holds despite the limitation of needing to assume homogeneous reaction conditions, whereas the reaction occurs at temperatures at which practically all polymer chains are collapsed, even as the diluted crosslinkers attach to them. The success of this model notwithstanding, it is onerous, even for regular monomers, to measure the large number of kinetic constants, and a combination of literature values and estimations based on the Price-Alfrey scheme are used instead²⁵. For new, custom synthesized molecules that are additionally expensive due to the cost of the dye molecules used and are only otherwise required in trace quantities, the standard means of measuring all the reaction rate constants required by the full terminal copolymerization model is impractical. Nevertheless, the kinetic parameters remain valuable, for example, combining approximations to the pseudo-kinetic rate constant approach with consumption data has been used to ensure the formation of particles with homogeneous crosslink density distributions.²⁴ Taken together, these studies underscore the importance of establishing the kinetic parameters for the new functional crosslink molecules, ideally without requiring the synthesis of large quantities of these relatively costly molecules.

Here, we demonstrate that it is possible to extract reliable quantitative information from the average localization probability density curves obtained by single molecule localization microscopy measurements of swollen PNiPAm microgels. Specifically, we conduct Direct Stochastic Optical Reconstruction Microscopy (dSTORM)^{26,27} measurements of dye tagged crosslink molecules to obtain relative two-dimensional localization probability density curves. Two classes of dyes are combined with acrylamide and methacrylamide variants of the crosslinker molecules. Three dimensional localization probability curves are obtained from the 2D curves while taking into account the exponential decay of the excitation intensity profile. The 3D probability density curves are combined with the volumetric evolution of the particles with time, obtained from dynamic light scattering data, to predict the dye tagged monomer consumption as a function of time. The predicted consumption profiles are found to be in good agreement with consumption curves measured analytically using UV-Vis spectroscopy. The consumption curves, along with consumption curves for NiPAm and BIS, are fit to a terminal copolymerization model to extract reaction rate constants for homopropagation and crosspropagation for the functional crosslinker with NiPAm and BIS. Specifically, we apply Bayesian regression using a Markov chain technique²⁸ to robustly quantify rate parameters and their uncertainties, thereby avoiding the difficulties associated with parameter estimation from conventional high-dimensional nonlinear fits²⁹. These reaction rate parameters, which are otherwise difficult to estimate due to the relative expense of the molecules, are expected to be useful for future ex-

periments, in particular those related to the study of spatial variations in crosslink density in gels.

2 Methods

2.1 Materials and Reagents

A detailed list of chemicals and reagents is provided in the ESI[†].

2.2 Cross-linker synthesis and characterization

Details of the synthesis of all the cross-linkers reported in the paper and their characterization is provided in the ESI[†]. We denote the methacrylamide and the acrylamide variants as BMA and BA, respectively. The dye tagged crosslinkers are denoted by crosslinker@dye.

2.3 Microgel synthesis

Microgels were synthesised as per a protocol described in the literature¹⁷. Briefly, for the 1:500 [crosslinker@dye]:[BIS] samples, 113 mg NiPAm (1 mmol), 3.05 mg BIS (0.02 mmol), 0.24 mg CTAB (0.66 μmol), and 40 nmol of crosslinker@dye were combined with H₂O to make a final reaction volume of $V_f = 8.25\text{ml}$ in a 25 ml round bottom flask equipped with a septum and an Ar gas inlet/outlet. The mixture was degassed for 40 min. The flask was then placed in a water bath at 75°C for 40 min, and 100 μl of a 10.7 mg/ml V-50 solution (3.95 μmol) was injected to initiate the polymerization. Under a mild Ar stream, aliquots (100 μl) were drawn from the reaction in regular intervals (2.5, 5, 7.5, 10, 12.5, 15, 20, 30, 40 and 70 min) and were transferred quickly (<5 sec) into ice-water cooled 1 dram vials containing 0.1 mg of hydroquinone (inhibitor). For the DLS measurements, the aliquots were passed through a 1 μm glass fiber syringe filter (Pall Laboratory), sonicated for 1 min at room temperature and diluted to concentrations sufficiently low for the prevention of multiple scattering. The main reactor itself was quenched in ice-water after 1.5 hours.

For the synthesis of 1:100 [crosslinker@Rh]:[BIS] samples, the reactions were scaled up approximately 6.06x. Briefly, 684 mg NiPAm, 18.3 mg BIS, 1.44 mg CTAB, 0.2 μmol of BA@Rh or BMA@Rh and H₂O were combined at a final reaction volume of $V_f = 50\text{ml}$ into a 100 ml three-neck round bottom flask equipped with a septum, Ar gas inlet/outlet and degassed for 40 min. After 40 min of equilibration at 70°C the reaction was initiated with 500 μl of a 12.97 mg/ml V-50 solution. Under a mild Ar stream, aliquots (2ml) were drawn from the reaction in regular intervals (2.5, 5, 7.5, 10, 12.5, 15, 20, 30, 40 and 70 min) and were transferred quickly (<5 sec) into ice-water cooled 1 dram vials containing 1 mg of hydroquinone. 1.75 ml of these aliquots were diluted 2x with H₂O, placed in 4 ml ultracentrifugation tubes and spun down at 35k RPM at 4°C. The supernatants were further diluted to concentrations appropriate for analytical characterization with HPLC and UV-Vis spectroscopy. Dispersions for DLS measurements of the precipitated aliquots were prepared following the above reported procedure.

2.4 dSTORM

2.4.1 Sample preparation.

Samples for super resolution imaging were prepared by casting 100 μl of 0.01% w/v microgel dispersions on polylysine coated circular glass coverslips (Mattek, 35 mm Dish, No. 1.5 Coverslip, 14 mm Glass Diameter, Uncoated). Before imaging, microgels were reconstituted in STORM buffer containing mercaptoethanol, glucose oxidase and catalase for at least 30 min (all reagents purchased from Sigma and buffer prepared according to Nikon N-STORM Sample Preparation Protocol).

2.4.2 Image acquisition.

dSTORM images were acquired with a CFI Apo TIRF 100x objective (1.49 NA) on a Nikon Ti-E inverted microscope equipped with a Nikon N-STORM system and a Hamamatsu sCMOS. The setup was controlled by Nikon NIS-Elements AR software with an N-STORM module. The dSTORM image was acquired using a STORM filter cube (Nikon) and the sCMOS camera. A single dSTORM experiment involved 60,000 cycles of continuous acquisition, 10 ms per cycle. All images were acquired in oblique illumination, applied using the TIRF illuminator of the microscope.

2.4.3 Image reconstruction.

dSTORM images were reconstructed using the imageJ plugin, thunderSTORM³⁰. Pre-processing filters were used to localize molecules in each frame of a dSTORM experiment. A wavelet filter (B-spline order = 3, B-spline scale = 2.0) was used to filter out noise and enhance features that corresponded to a localization event. Threshold values for a localization event were set as a multiple of the standard deviation of the intensity distribution in each wavelet filtered frame and the 'local maximum' method was used to determine the approximate positions of each event. Sub-pixel localization of molecules was achieved via a least squares fit of an integrated Gaussian PSF to each event.

The ensemble localization data was filtered on the basis of values for sigma, intensities and uncertainties³¹. The uncertainty limits were set to 30nm in the 1:500 cases and 80nm for the 1:100 cases. Higher uncertainties in the microgels with higher dye concentrations were a byproduct of the extensive bleaching required to induce single molecule switching. The molecules surviving the bleaching emitted fewer photons, which resulted in the higher uncertainties ($\Delta x \propto \frac{1}{\sqrt{N}}$). The inbuilt cross-correlation algorithm was used to correct for drift during the acquisition.

2.4.4 Localisation density calculation.

The ELKI³² implementation of the clustering algorithm, DB-SCAN³³, was used to segregate the data of each individual microgel from the ensemble localization data. A 'net microgel' was constructed by superimposing the data of each microgel. The localizations in the 'net microgel' were binned as per their distance from the center. Each bin was weighted by the area of the bin, treated as the difference in areas of the inner and outer circles of the bin. To reconstruct the 3D distribution from the obtained 2D storm data, the projection of a weighted 3D sigmoid onto the 'xy', or focal plane, was fitted to the obtained dSTORM data. The weight function used was an exponential function with

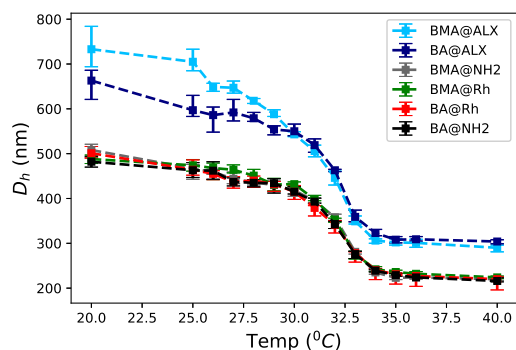


Fig. 1 Hydrodynamic radii measured by dynamic light scattering versus temperature for microgels containing trace quantities of methacrylamide (BMA) and acrylamide (BA) variants of dye tagged crosslinkers, which are designated by crosslinker@dye. Dyes shown are Alexa647 (ALX), a cyanine dye; and Carboxytetramethylrhodamine (Rh), a Rhodamine dye. The unreacted amine functional group in an untagged crosslinker is designated by NH2.

a decay constant that corresponds to that of the excitation profile of the evanescent wave along the 'z', or optical axis, in the tirf setup³⁴. The fit parameters obtained were then used to plot the unweighted 3D function.

2.4.5 Bayesian regression.

The estimates of the rate constants and related parameters are obtained via a Bayesian regression model²⁸, in which the probability distributions of the unknown fit parameters given the data ($P(\vec{\theta}, \sigma_R | \{t_{ij}, C_{ij}\})$) are obtained from the following relationship that holds under the assumption of a uniform prior distribution.

$$P(\vec{\theta}, \sigma_R | \{t_{ij}, C_{ij}\}) \propto P(\{t_{ij}, C_{ij}\} | \vec{\theta}, \sigma_R) \quad (1)$$

Here, $\vec{\theta}$ represents the set of fit parameters in the model, and, as per the results and discussions section, takes one of the following values $\{k_{33}, Q_3, e_3, R_{total}\}$, $\{k_{33}, Q_3, e_3, \alpha, R_{total}\}$, or $\{k_{13}, k_{23}, k_{31}, k_{32}, k_{33}, R_{total}\}$; $\{t_{ij}, C_{ij}\}$ represents the experimental consumption data where 'i' denotes the monomer and 'j' is the data index for the corresponding monomer; and $P(\{t_{ij}, C_{ij}\} | \vec{\theta}, \sigma_R)$ is the probability distribution of the data given the parameters and is assumed to be a Gaussian distribution of residuals with an unknown variance (σ_R). The residual is obtained as the difference between the consumption data ($\{t_{ij}, C_{ij}\}$) and the solution, $f(t, \vec{\theta})$, obtained from the terminal co-polymerization model for a given set of parameters. $P(\{t_{ij}, C_{ij}\} | \vec{\theta}, \sigma_R)$ is given by:

$$P(\{t_{ij}, C_{ij}\} | \vec{\theta}, \sigma_R) = \prod_i \frac{1}{\sqrt{2\pi}\sigma_R} \left[\exp \frac{-(C_{ij} - f(t_{ij}, \vec{\theta}))^2}{2\sigma_R^2} \right] \quad (2)$$

The sampling of these distributions for the parameters is achieved through the implementation of a Markov chain algorithm. The algorithm invokes random walks in the multi-dimensional parameter space in which a proposed step, from $\vec{\theta}_n$ to $\vec{\theta}_{n+1}$, is accepted if $P(\{t_{ij}, C_{ij}\} | \vec{\theta}_{n+1}, \sigma_R) \geq P(\{t_{ij}, C_{ij}\} | \vec{\theta}_n, \sigma_R)$. If the condition is not satisfied, the proposed step is accepted with probability $\frac{P(\{t_{ij}, C_{ij}\} | \vec{\theta}_{n+1}, \sigma_R)}{P(\{t_{ij}, C_{ij}\} | \vec{\theta}_n, \sigma_R)}$. The sampled distributions of the pa-

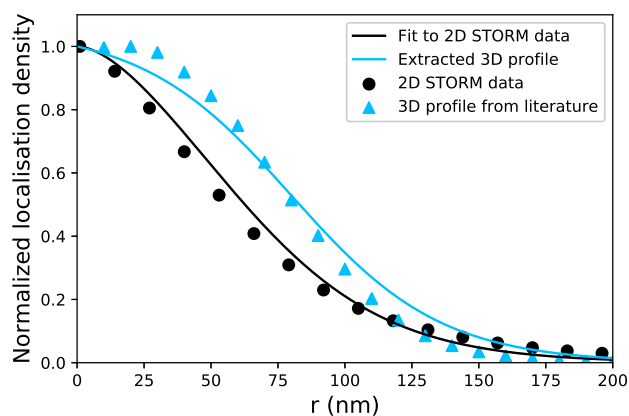


Fig. 2 Extraction of 3D localization probability density profiles (blue trace) from 2D STORM data (black circles), fit with a projected 3D profile after correcting for the TIRF excitation profile (black curve) and comparison with high resolution 3D data from the literature (blue triangles).

rameters are obtained from 15 random walks, each traversing 5000 steps. Final estimates of the parameters were obtained from a maximum likelihood estimate that corresponded to the maximum in the normalized probability distribution function. Error bounds are estimated from a 70 percent confidence interval estimate obtained from the corresponding cumulative distribution.

3 Results and discussion

PNiPAm microgels were synthesized at 75°C with 2 mol% BIS and 4×10^{-3} mol% of the dye-tagged crosslinker. The functional crosslinker has been previously reported¹⁷ as its methacrylamide (BMA) variant. Here we also present and use the acrylamide (BA) variant of the crosslinker. Figure 1 shows representative examples of the impact of attaching cyanine (Alexa647, denoted as ALX) and rhodamine (Carboxytetramethylrhodamine, denoted as Rh) dye molecules to BMA and BA crosslinker variants on microgel radius and swelling ratio (see ESI[†] for additional examples). The Cyanine dyes result in larger microgels than Rhodamines. By comparison, for a given dye, the contrast between using BMA and BA is small. This contrast is noteworthy since the change from BMA to BA would be expected to play a greater role than the dangling dye substituent, and we surmise that the cyanine dye interferes with the process of chain growth, with a net impact similar to varying surfactant and initiator amounts.

2D localization probability density profiles as a function of projected radius are obtained by performing dSTORM measurements on the microgels. The 3D radial profile is reconstructed from the 2D profile using a modification of the procedure described in the literature¹²; specifically, we find it necessary to weight the 3D test functions by the tirf excitation profile prior to projecting onto the 2D plane and fitting. This modified extraction of 3D profiles is validated by the agreement with directly measured 3D profiles for BMA@Alx crosslink molecules previously reported in the literature using W-4PiSMSN¹⁷ (see Figure 2).

To facilitate the comparison of predicted dye tagged crosslinker consumption with values measured by independent analytical techniques, the cheaper Carboxytetramethylrhodamine dye was

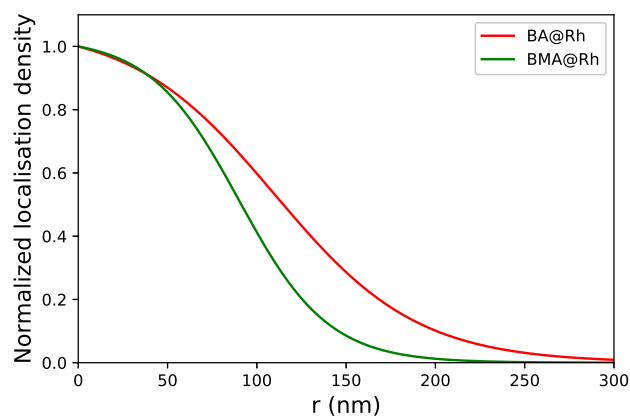


Fig. 3 Radial relative localization probability density profiles for Rhodamine tagged BMA and BA crosslinkers, plotted as green and red traces, respectively.

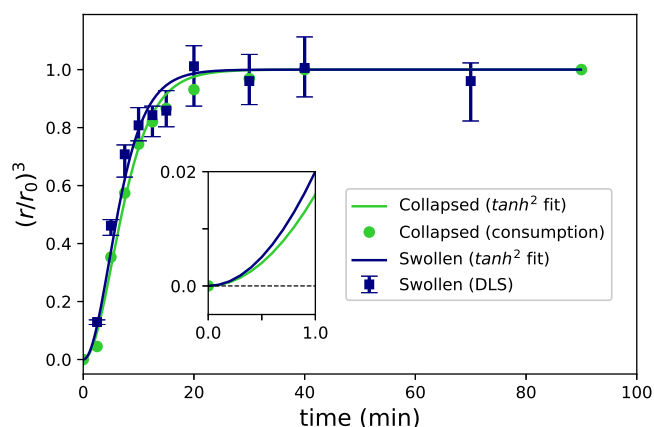


Fig. 4 Normalised volumetric evolution of microgels in the (a) swollen state obtained from dynamic light scattering data (dark blue squares) and (b) collapsed state estimated from consumption of NiPAm (green circles). The solid traces are the corresponding \tanh^2 fits. Here, r and r_0 are the instantaneous and final particle radii, respectively. The inset shows that the slope approaches zero at the origin.

used and some synthesis parameters changed. To slow the kinetics down, we shifted to a synthesis temperature of 70°C. To improve signal to noise we increased the functional crosslinker concentration to 2×10^{-2} mol%. Figure 3 shows the resultant 3D radial distribution curves, both of which are found to be sigmoidal.

We first calculate $C(r_s)$, the fraction of dye tagged crosslinker that remains unreacted when the average radius of the growing microgel particles in the swollen state is r_s . We assume that all of the consumed dye tagged crosslinker is incorporated into the microgel particles, and denote the final radius by R , and the radial relative localization probability density function by $\rho(r_s)$. $C(r_s)$ is then given by:

$$C(r_s) = 1 - \frac{\int_0^{r_s} 4\pi r_s^2 \rho(r_s) dr_s}{\int_0^R 4\pi r_s^2 \rho(r_s) dr_s} \quad (3)$$

To convert $C(r_s)$ into consumption, we use the volumetric evo-

lution of the swollen particles shown by the dark blue squares in Figure 4, where the instantaneous volume is normalised by the final volume. The form of the curve shows a rapid evolution and a final saturation. This is consistent with the previous literature²⁴, which itself features a zero slope at the origin, and thus an incubation period for very short times. To establish the form of our data at such short times, where DLS measurements are less reliable, we turn to the established model for ensemble averaged growth.²³ As the NiPAm rich chains grow in the solution phase at temperatures far above the volume phase transition temperature, they collapse and precipitate on the nucleated collapsed gel particles, creating a link between consumption and radial position within the ensemble average of the microgel particles as they grow in the collapsed form. For microgels that consist primarily of PNiPAm, 98% in our case, if we assume uniform polymer density in the collapsed state, the volume of the collapsed gel particle normalised by its final volume, $(\frac{r(t)}{r_0})^3$, is equal to the fraction of NiPAm monomer consumed. Here, r and r_0 are the instantaneous and final particle radii, respectively. The volumetric evolution of the collapsed particles calculated in this manner (green circles in Figure 4) clearly shows an initial incubation period prior to rapid evolution as represented by the slope approaching zero at zero time; we fit the full curve to a \tanh^2 function (green trace). Since the inner core of the microgel has higher crosslink density, for shorter times we expect a proportionality between the volumetric evolution of particles in the collapsed and swollen states. We thus fit the volumetric evolution of the swollen microgels to a \tanh^2 function as well (blue trace). We note that the volumetric evolution of the swollen and collapsed forms do not fall onto a master \tanh^2 curve; the swollen and collapsed forms evolve at different rates.

Figure 5 shows the predicted consumption curves for the BA@Rh and BMA@Rh crosslinkers. The predictions are contrasted to consumption rates measured by UV-Vis absorbance of aliquots taken from the respective reaction mixtures at regular intervals. We ascribe the compelling accuracy of the predictions to multiple morphological factors. We use relative densities within structures that are not extended and complex. The microgel particles themselves are well isolated and easily distinguishable from the background. The density profiles are repetitive and contained within geometrically stereotypical spherical structures, which facilitates averaging. Finally, we prefunctionalize the fluorophores prior to synthesis. Taken together, these factors serve to mitigate the potentially deleterious effects of labelling inefficiency, and variations in the photophysics of the fluorophores such as photobleaching and multiple blinking. Interestingly, in a recent review, Baddeley and Bewersdorf³⁵ have commented that the bulk of the most biologically relevant localization microscopy results have come from morphologies with similar characteristics.

To exemplify the utility of quantitatively predicting consumption curves for the dye tagged crosslinkers, we calculate the rate constants of homo and cross-propagation of BMA@Rh with NiPAm and BIS. Since low-concentration solution polymerization kinetics captures the consumption curves of all three monomers, we measure the consumption curves of NiPAm and BIS using high performance liquid chromatography (HPLC). Using lit

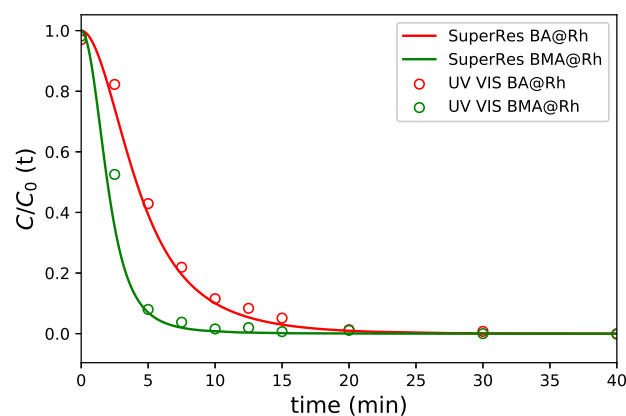


Fig. 5 Comparison of consumption rates predicted from dSTORM data for BMA@Rh (green trace) and BA@Rh (red trace) with rates from UV-Vis measurements of the supernatant in the reactor (open circles).

erature values for the rate constants that do not involve the new compound²⁵, we apply an established explicit terminal copolymerization model²³ to fit the consumption curves and extract the five desired rate constants. Briefly, this model performs the monomer mass balance given below:

$$\frac{d[N_i]}{dt} = -\left(\sum_j \kappa_{ji}\phi_j\right)[N_i][R_{total}] \quad (4)$$

where the subscript $i = 1, 2, 3$ refers to NiPAm, BIS and dye tagged crosslinker, respectively; κ_{ji} is the rate constant of monomer i propagating with radical j ; ϕ_j is the radical fraction of component j at any given time, and R_{total} is the total concentration of radicals in the system, which is assumed to be constant as per the steady state approximation. The summation term can be interpreted to be the pseudo-kinetic rate constant for any given monomer.

While calculating the five unknown rate constants, we assume that their values are constrained by the Price-Alfrey scheme³⁶. Briefly, the Price-Alfrey scheme is an empirical method that asso-

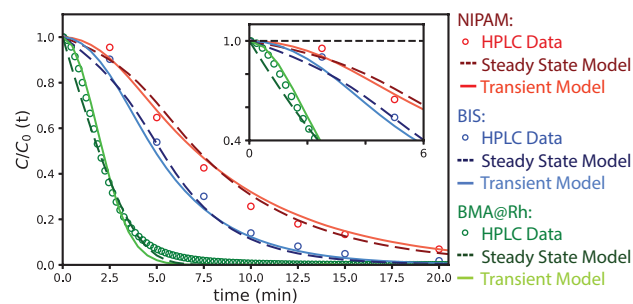


Fig. 6 Fits to consumption data (open circles) for NiPAm (red), BIS (blue) and BMA@Rh (green) using a steady state terminal copolymerization model (dashed lines) and a modified transient model (solid lines) in which the total radical concentration is assumed to have a \tanh functional form with time. Both models are constrained to be consistent with the Price-Alfrey scheme. The inset shows that the transient model better captures early time behavior.

Table 1 Rate constants for BMA@Rh calculated using a terminal copolymerization model implementing the Price-Alfrey scheme. All rate constant units are in $[L\ mol^{-1}\ s^{-1}]$. Parameters are reported as Mean [+Upper Error Bound, -Lower Error Bound]

Parameter	Price Alfrey (constant R_{total})	Price Alfrey (time varying R_{total})
k_{33}	9.0 [+37, -0.1]	4.8 [+2.6, -0.7]
Q_3	3.2 [+0.15, -0.50]	2.1 [+0.4, -0.15]
e_3	2.1 [+0.5, -0.15]	1.63 [+0.2, -0.45]
k_{13}	7.90×10^5 [$+8.5 \times 10^4$, -9.0×10^4]	9.02×10^5 [$+1.0 \times 10^5$, -9.0×10^4]
k_{23}	1.21×10^5 [$+1.7 \times 10^4$, -1.1×10^4]	1.56×10^5 [$+1.9 \times 10^4$, -1.5×10^4]
k_{31}	3.0 [+39, -1.0]	0.8 [+0.4, -0.4]
k_{32}	5.0 [+43, -0.2]	1.1 [+1.2, -0.3]
k_{33}	9.0 [+37, -0.1]	4.8 [+2.6, -0.7]
<i>rmse</i>	0.031	0.026

ciates individual monomers with two constants, Q and e, that can then be used to estimate reactivity ratios for free radical copolymerization. Since the Q and e parameters for NiPAm and BIS are known from the literature²⁵, the task of evaluating the five rate constants reduces to evaluating three parameters, Q_3 , e_3 and k_{33} (See ESI[†] for equations relating the rate constants to the three parameters). The parameters Q_3 , e_3 and k_{33} were determined via a Bayesian regression approach²⁸ which simultaneously minimized the residuals of the fits to the experimental consumption data of all three monomer species (see ESI[†] for plots). Since this approach provides the probability distributions of fit parameters which turn out to be highly asymmetric in certain cases, we report the maximum likelihood estimate, and the error bounds are calculated using confidence intervals for the parameters. The calculated parameters and the root mean square error (rmse) from the fits to the relative concentration consumption data are listed in Table 1. The fits (dashed lines) and consumption data (open circles) are shown in Figure 6.

Next, we consider the early time behavior of the consumption data, shown in the inset of Figure 6. The terminal copolymerization model assumes a constant value for R_{total} , and this model is unable to fully capture the early time behavior of the consumption data due to the presence of the fast-reacting BMA@Rh monomer. We therefore consider a modified transient model in which the R_{total} term from Equation 4 is multiplied by a $\tanh(\alpha t)$ factor. As before, the parameters are determined via the Bayesian regression model (see Table ESI[†] for plots). The resultant rate constants and rmse errors for the best fit parameters are summarized in Table 1, while the fits to the consumption data (solid lines) are shown in Figure 6. The modified transient model works better in describing the data, as demonstrated by the reduction in estimated errors of the rate constant parameters, as well as a reduction in the root mean squared error values of the fits to the consumption data. We ascribe this improvement to the use of the $\tanh(\alpha t)$ factor, since it is known that the total radical concentration evolves with such a functional form³⁷.

Finally, we considered the possibility that the Price-Alfrey model does not hold for BMA@Rh. However, we found that although the use of five independent kinetic rate constants results in a marginal improvement in the rmse value, which is expected for an increase in number of free parameters, several of the determined rate constants themselves became ill-defined, with large

70 percent confidence intervals relative to the respective means, and we did not consider this possibility further.

4 Conclusions

In summary, we have demonstrated that the morphology of colloidal microgels is uniquely suited to allow for the extraction of quantitative information from single molecule localization microscopy. Averaged and normalised localization probability density curves can be combined with volume evolution data to accurately predict consumption of dye tagged monomer as a function of time. These curves, when combined with consumption data of the other monomers, can in turn be used to extract kinetic rate constants for homopropagation and crosspropagation. These constants, which are otherwise difficult to measure due to practical cost considerations, are expected to be useful in morphological studies of colloidal and bulk gels, in particular the impact on properties of spatial variations in crosslink density.

Conflicts of interest

There are no conflicts to declare.

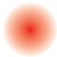
Acknowledgements

This work is based in part upon work supported by the National Science Foundation under grant no. 1654599 and instrumentation acquired under grant no. 1725984. Acknowledgement is made to the Donors of the American Chemical Society Petroleum Research Fund for partial support of this research. STORM data collection was performed in the Light Microscopy Facility and Nikon Center of Excellence at the Institute for Applied Life Sciences, University of Massachusetts Amherst with support from the Massachusetts Life Science Center. We thank Prof. Chang Ryu and Prof. Edmund Palermo for graciously allowing use of their laboratory facilities. RPI staff at the CBIS Proteomics and Analytical Biochemistry Cores are acknowledged for facilitating part of the experimental work.

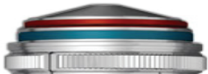
Notes and references

- 1 S. W. Hell, *Angewandte Chemie-International Edition*, 2015, **54**, 8054–8066.
- 2 E. Betzig, *Angewandte Chemie - International Edition*, 2015, **54**, 8034–8053.

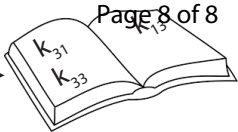
- 3 P. Delcanale, I. Voets and L. Albertazzi, *Nature Reviews Chemistry*, 2019, **3**, 68–84.
- 4 B. Harke, C. K. Ullal, J. Keller and S. W. Hell, *Nano Letters*, 2008, **8**, 1309–1313.
- 5 C. K. Ullal, R. Schmidt, S. W. Hell and A. Egner, *Nano Letters*, 2009, **9**, 2497–2500.
- 6 K. Friedemann, A. Turshatov, K. Landfester and D. Crespy, *Langmuir*, 2011, **27**, 7132–7139.
- 7 M. A. Lauterbach, C. K. Ullal, V. Westphal and S. W. Hell, *Langmuir*, 2010, **26**, 14400–14404.
- 8 R. M. P. da Silva, D. van der Zwaag, L. Albertazzi, S. S. Lee, E. W. Meijer and S. I. Stupp, *Nature Communications*, 2016, **7**, 11561.
- 9 Z. Qiang, K. M. Shebek, M. Irie and M. Wang, *ACS Macro Letters*, 2018, **7**, 1432–1437.
- 10 A. J. Berro, A. J. Berglund, P. T. Carmichael, J.-S. Kim and J. A. Liddle, *ACS NANO*, 2012, **6**, 9496–9502.
- 11 M. Wang, J. M. Marr, M. Davanco, J. W. Gilman and J. A. Liddle, *Materials Horizons*, 2019, **6**, 817–825.
- 12 A. P. H. Gelissen, A. Oppermann, T. Caumanns, P. Hebbeker, S. K. Turnhoff, R. Tiwari, S. Eisold, U. Simon, Y. Lu, J. Mayer, W. Richtering, A. Walther and D. Woell, *Nano Letters*, 2016, **16**, 7295–7301.
- 13 S. Bergmann, O. Wrede, T. Huser and T. Hellweg, *Physical Chemistry Chemical Physics*, 2018, **20**, 5074–5083.
- 14 G. M. Conley, S. Nojd, M. Braibanti, P. Schurtenberger and F. Scheffold, *Colloids and Surfaces A-Physicochemical and Engineering Aspects*, 2016, **499**, 18–23.
- 15 G. M. Conley, P. Aebischer, S. Nojd, P. Schurtenberger and F. Scheffold, *Science Advances*, 2017, **3**, year.
- 16 S. J. Sahl, S. W. Hell and S. Jakobs, *Nature Reviews Molecular Cell Biology*, 2017, **18**, 685–701.
- 17 A. A. Karanastasis, Y. Zhang, G. S. Kenath, M. D. Lessard, J. Bewersdorf and C. K. Ullal, *Materials Horizons*, 2018, **5**, 1130–1136.
- 18 E. Siemes, O. Nevskiy, D. Sysoiev, S. K. Turnhoff, A. Oppermann, T. Huhn, W. Richtering and D. Woell, *Angewandte Chemie-International Edition*, 2018, **57**, 12280–12284.
- 19 M. Stieger, W. Richtering, J. S. Pedersen and P. Lindner, *Journal of Chemical Physics*, 2004, **120**, 6197 – 6206.
- 20 S. Matsui, Y. Nishizawa, T. Uchihashi and D. Suzuki, *ACS Omega*, 2018, **3**, 10836–10842.
- 21 Y. Nishizawa, S. Matsui, K. Urayama, T. Kureha, M. Shibayama, T. Uchihashi and D. Suzuki, *Angewandte Chemie-International Edition*, 2019, **0**.
- 22 O. L. J. Virtanen and W. Richtering, *Colloid and Polymer Science*, 2014, **292**, 1435 – 1536.
- 23 T. Hoare and D. McLean, *Journal of Physical Chemistry B*, 2006, **110**, 20327 – 20336.
- 24 R. Acciaro, T. Gilányi and I. Varga, *Langmuir*, 2011, **27**, 7917–7925.
- 25 T. Hoare and D. McLean, *Macromolecular Theory and Simulations*, 2006, **15**, 619 – 632.
- 26 M. Heilemann, S. van de Linde, M. Schüttpelz, R. Kasper, B. Seefeldt, A. Mukherjee, P. Tinnefeld and M. Sauer, *Angewandte Chemie International Edition*, 2008, **47**, 6172–6176.
- 27 M. J. Rust, M. Bates and X. Zhuang, *Nature Methods*, 2006, **3**, 793–796.
- 28 A. Gelman, J. Carlin, H. Stern, D. Dunson, A. Vehtari and D. Rubin, *Bayesian Data Analysis, Third Edition*, Taylor & Francis, 2013.
- 29 K. S. Brown and J. P. Sethna, *Phys. Rev. E*, 2003, **68**, 021904.
- 30 M. Ovesný, P. Křížek, J. Borkovec, Z. Švindrych and G. M. Hagen, *Bioinformatics*, 2014, **30**, 2389–2390.
- 31 P. Křížek, I. Raška and G. M. Hagen, *Opt. Express*, 2011, **19**, 3226–3235.
- 32 E. Schubert and A. Zimek, *CoRR*, 2019, **abs/1902.03616**, year.
- 33 M. Ester, H.-P. Kriegel, J. Sander and X. Xu, *Proceedings of the Second International Conference on Knowledge Discovery and Data Mining*, 1996, pp. 226–231.
- 34 M. Martin-Fernandez, C. Tynan and S. Webb, *Journal of Microscopy*, 2013, **252**, 16–22.
- 35 D. Baddeley and J. Bewersdorf, *Annual Review of Biochemistry*, Vol 87, 2018, vol. 87, pp. 965–989.
- 36 T. Alfrey Jr. and C. C. Price, *Journal of Polymer Science*, 1947, **2**, 101–106.
- 37 P. J. Flory, *Principles of polymer chemistry.*, Cornell University Press, 1953.



Soft Matter



Super-resolution microscopy



Rate constants